



## Role of Catalytic Conversions of Ethylene Carbonate, Water, and HF in Forming the Solid-Electrolyte Interphase of Li-Ion Batteries

**Martins, Milena; Haering, Dominik; Connell, Justin G.; Wan, Hao; Svane, Katrine L.; Genorio, Bostjan; Farinazzo Bergamo Dias Martins, Pedro; Lopes, Pietro P.; Gould, Brian; Maglia, Filippo**

*Total number of authors:*  
16

*Published in:*  
ACS Catalysis

*Link to article, DOI:*  
[10.1021/acscatal.3c01531](https://doi.org/10.1021/acscatal.3c01531)

*Publication date:*  
2023

*Document Version*  
Publisher's PDF, also known as Version of record

[Link back to DTU Orbit](#)

### *Citation (APA):*

Martins, M., Haering, D., Connell, J. G., Wan, H., Svane, K. L., Genorio, B., Farinazzo Bergamo Dias Martins, P., Lopes, P. P., Gould, B., Maglia, F., Jung, R., Stamenkovic, V., Castelli, I. E., Markovic, N. M., Rossmeisl, J., & Strmcnik, D. (2023). Role of Catalytic Conversions of Ethylene Carbonate, Water, and HF in Forming the Solid-Electrolyte Interphase of Li-Ion Batteries. *ACS Catalysis*, 13(13), 9289-9301. <https://doi.org/10.1021/acscatal.3c01531>

---

### General rights

Copyright and moral rights for the publications made accessible in the public portal are retained by the authors and/or other copyright owners and it is a condition of accessing publications that users recognise and abide by the legal requirements associated with these rights.

- Users may download and print one copy of any publication from the public portal for the purpose of private study or research.
- You may not further distribute the material or use it for any profit-making activity or commercial gain
- You may freely distribute the URL identifying the publication in the public portal

If you believe that this document breaches copyright please contact us providing details, and we will remove access to the work immediately and investigate your claim.

# Role of Catalytic Conversions of Ethylene Carbonate, Water, and HF in Forming the Solid-Electrolyte Interphase of Li-Ion Batteries

Milena Martins, Dominik Haering, Justin G. Connell, Hao Wan, Katrine L. Svane, Bostjan Genorio, Pedro Farinazzo Bergamo Dias Martins, Pietro P. Lopes, Brian Gould, Filippo Maglia, Roland Jung, Vojislav Stamenkovic, Ivano E. Castelli, Nenad M. Markovic, Jan Rossmeisl, and Dusan Strmcnik\*



Cite This: *ACS Catal.* 2023, 13, 9289–9301



Read Online

ACCESS |



Metrics & More



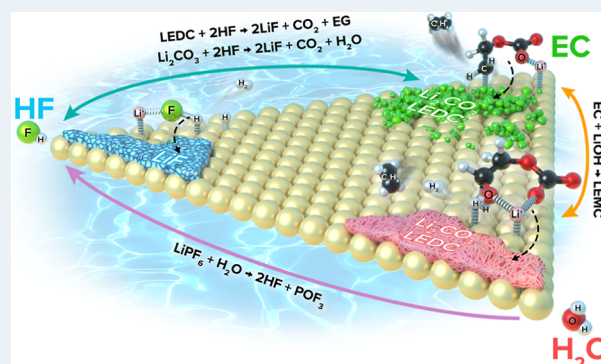
Article Recommendations



Supporting Information

**ABSTRACT:** Compared to aqueous electrolytes, fundamental understanding of the chemical and electrochemical processes occurring in non-aqueous electrolytes is far less developed. This is no different for Li-ion battery (LiB) electrolytes, where many questions regarding the solid-electrolyte interphase (SEI) on the anode side remain unanswered, including its chemical composition, the mechanism of formation, and its impact on LiB performance. Here, we present a detailed experimental and theoretical study of the electrochemistry of ethylene carbonate (EC) and its chemical relationship with trace amounts of water and HF across a vast range of electrode materials, from well-ordered single crystals to realistic graphite electrodes. We reveal the electrocatalytic nature of EC, HF, and water electro-reductions at all interfaces, and unveil the catalytic role of water in EC electroreduction. Moreover, we show that these reactions are connected in a closed cycle by chemical reactions that take place either at the electrode/electrolyte interface or in the bulk of the electrolyte and demonstrate that the composition of the SEI depends predominantly on the balance between the (electro)chemistry of EC, water, and HF.

**KEYWORDS:** Li-ion battery, solid-electrolyte interphase, electroreduction, ethylene carbonate, HF, water



## 1. INTRODUCTION

Increased demand for the utilization of renewable energy sources is driving the rapid development of energy storage technologies. With a substantial market in portable electronic devices and the transportation sector, Li-ion batteries (LiBs) are on the forefront of energy storage for mobile applications.<sup>1,2</sup> Despite their wide use and decades of research, LiBs still face enormous challenges related predominantly to the loss of performance over time.<sup>3–5</sup> It is commonly agreed that one of the most important drivers of efficiency loss at the anode side of LiBs is the solid-electrolyte interphase (SEI).<sup>6–8</sup> It is also accepted that the SEI is formed by the reduction of electrolyte components in the first charging cycle, resulting in a barrier against further electrolyte decomposition that still allows for good Li<sup>+</sup> ion conductivity.<sup>9–12</sup> Typical LiB electrolytes consist of lithium hexafluorophosphate (LiPF<sub>6</sub>) in linear (ethyl-methyl carbonate, EMC, or dimethyl carbonate, DMC) and cyclic (ethylene carbonate, EC) carbonate solvents.<sup>13–15</sup> As a result of these electrolyte constituents, the most frequently reported components of the SEI are LiF, Li<sub>2</sub>CO<sub>3</sub>, LiOH, Li<sub>x</sub>O, Li<sub>2</sub>C<sub>2</sub>O<sub>4</sub>, and lithium ethylene di-carbonate (LEDC),<sup>9,16–19</sup> which gives us the answer to what the SEI is comprised of. Yet, depending on the report, different combinations or different ratios of these SEI

compounds have been found.<sup>11,20–24</sup> In some cases, even the chemical nature of some of the compounds has been questioned. Most recently, in a detailed study by Wang et al., it has been suggested that lithium ethylene mono-carbonate (LEMC), rather than LEDC, is most likely the main organic component of the SEI.<sup>25</sup> In addition, one can also find several contradictory reports on where in the interphase these compounds can be found.<sup>7,11,26–28</sup> Much less common, however, are the answers to how and why these SEI-forming reactions happen, at least at the atomic/molecular level.<sup>29,30</sup> Compared to aqueous electrolytes, the fundamental understanding of the chemical and electrochemical processes occurring in non-aqueous electrolytes is, in general, far less developed. In the case of LiB electrolytes, such understanding is impeded by the enormous complexity introduced by the number of possible competing and interrelated (electro)-

**Received:** April 4, 2023

**Revised:** May 29, 2023

**Published:** June 27, 2023



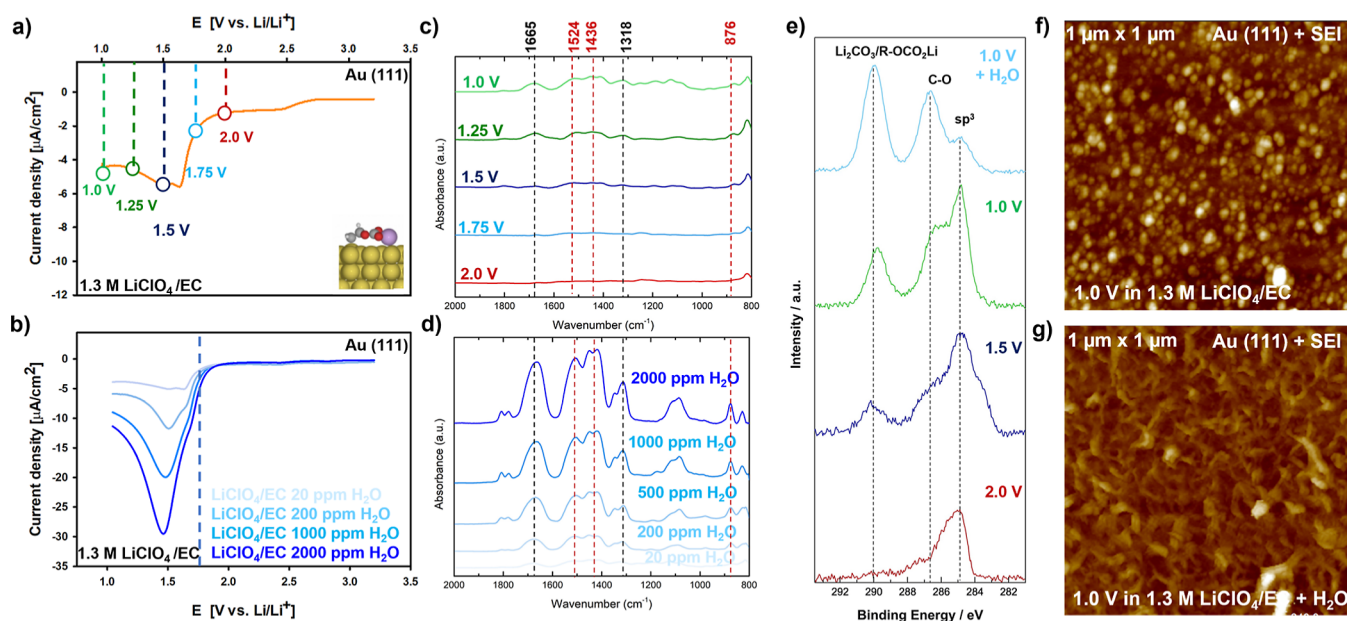


**Figure 1.** (a) Electrochemical response of Au(111) in 1.3 M LiClO<sub>4</sub>/EC; first scan, taken at 1 mV/s in the negative direction. (b) Dependence of the main electroreduction peak on Au(111) on the concentration of H<sub>2</sub>O in LiClO<sub>4</sub>/EC electrolyte (c) Evolution of FTIR spectra with the potential sweep at different potentials—snapshots were taken at 2.0, 1.75, 1.5, 1.25, and 1.0 V vs Li/Li<sup>+</sup>. (d) Evolution of FTIR spectra with changing water concentration in LiClO<sub>4</sub>/EC electrolyte after potential scan to 1 V. (e) C 1s XPS spectra of the Au(111) surface after potential scans to 2.0, 1.5, and 1.0 V. For comparison, the C 1s spectrum is also shown for the Au(111) surface after the potential scan to 1.0 V in the LiClO<sub>4</sub>/EC electrolyte containing 1000 ppm of H<sub>2</sub>O. (f) AFM image of the SEI formed on Au(111) after potential sweep at 1.0 V in the low water content (<20 ppm) LiClO<sub>4</sub>/EC electrolyte. (g) AFM image of the SEI formed on Au(111) after potential scan to 1.0 V in the high water content (1000 ppm) LiClO<sub>4</sub>/EC electrolyte.

chemical reactions that are determined by the components of the electrolyte, and further complicated by the nature and morphology of the electrode material.<sup>13</sup> In fact, the understanding of the role of the electrode surface, potential, and chemical composition of the electrolyte in directing SEI formation is rather limited. As a result, the physical and chemical properties of the SEI are the subject of an ongoing and vigorous debate, oftentimes pointing to substantially different natures, structures, and origins of the main SEI components.<sup>9</sup>

The employment of model systems, which have advanced the fundamental understanding of aqueous systems, has been rarely attempted for Li-ion battery systems. By reducing the number of parameters, and hence the complexity, it is possible to bring theory closer to experiment. We have recently employed our surface science-based approach to study the electrochemistry of two common components of LiB electrolytes—HF and H<sub>2</sub>O—as well as their chemical relationship.<sup>31,32</sup> We have demonstrated that potential-dependent reorganization of the double layer enables the electrocatalytic transformation of these two species into their corresponding reaction products.

The study reported herein focuses on the electrochemical reduction of EC, H<sub>2</sub>O, and HF and their chemical relationships. The products of EC reduction in low and high-water content electrolytes were first investigated on model metal systems, i.e., single crystals of Au(111), Ir(111), Pt(111), Cu(111), and graphene on Pt(111). The utilization of model systems allows us to more accurately assess the contribution of individual chemical and electrochemical reactions to the formation of the SEI and relate them to the work functions of the individual surfaces. By a combined experimental/computational approach, we established that all the SEI-

forming electrochemical reactions, i.e., EC, H<sub>2</sub>O, and HF reduction, follow a general electrocatalytic pathway. This pathway does not originate from typical interactions of the reactants with the electrode surface, but rather from the potential-dependent structure of the double layer. Furthermore, we show that the electrochemical reactions are linked through chemical reactions between individual components of the electrolyte and the SEI. Most prominently, impurity water serves as a catalyst for the formation of LEDC and Li<sub>2</sub>CO<sub>3</sub>, the most abundant components of the SEI.

The knowledge gained from model systems was then utilized on more complex, carbon-based materials ranging from basal plane- and edge-exposed highly ordered pyrolytic graphite (HOPG) to real graphite anodes. We show that the complex systems follow the same principles as the model systems, with no changes to the elementary steps of SEI formation. However, it is the balance between these elementary reactions involving HF, H<sub>2</sub>O, and EC that ultimately determines the composition and the morphology of the SEI and can, depending on the experimental conditions, lead to vastly different outcomes even in the same electrolyte. We believe that this general mechanism explains the vast discrepancies between different reports on the SEI found in the literature and further provides a roadmap for how to create SEIs of desired composition and morphology for improved battery performance and lifetime.

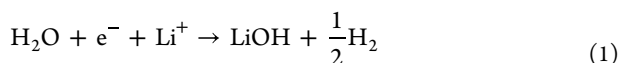
## 2. RESULTS AND DISCUSSION

**2.1. Electrochemistry of H<sub>2</sub>O and EC on Metal Single Crystals.** We start by investigating the electrochemical reduction of 1.3 M LiClO<sub>4</sub>/EC electrolyte on metal single crystal electrodes. As a representative of metal surfaces, we focus here predominantly on Au(111). This surface served as our model system for the present study as well as the reference



system for establishing our complete methodology that was then used on other samples. Similar results/trends were observed on Pt(111), Ir(111), and Cu(111) and are summarized in the [Supporting Information](#). The choice of single solvent electrolytes over LiPF<sub>6</sub>/EC/EMC (LP57, commonly used in LiB electrolytes) was done to minimize the complexity of the system and allow the isolated study of the electrochemical response of each individual component. Furthermore, LiClO<sub>4</sub>/EC was chosen specifically to avoid interference from HF, which is always present in LiPF<sub>6</sub>-based electrolytes in millimolar concentrations as an impurity. As reported in our recent study,<sup>31</sup> HF is the most reactive component in those electrolytes and gets electrochemically reduced before any other electrolyte component, effectively overriding all other processes that happen at more negative potentials.

[Figure 1a](#) shows a typical voltammogram for the Au(111) surface in 1.3 M LiClO<sub>4</sub>/EC electrolyte, recorded at 1 mV/s. Two overlapping peaks are observed in the cathodic scan at 1.7 and 1.5 V (all potentials are reported vs Li/Li<sup>+</sup>). The anodic scan is rather featureless, indicating irreversibility of the process. The shape of the curve as well as the second scan (see [Figure S1a](#)), indicates a partial passivation of the surface, which is complete only after several scans. The atomic force microscopy (AFM) image after the first potential scan to 1 V clearly shows the presence of a granular film on the gold surface ([Figure 1f](#)). It seems that the porosity of the film gives sufficient access of the electrolyte to the surface leading to diminished, but still significant, currents in subsequent scans. As shown in [Figure 1b](#), we observed a gradual increase of the reduction currents when increasing the water content in the electrolyte. This demonstrates that water is reduced in the 1.25–1.75 V potential window on Au(111) via the hydrogen evolution reaction (HER) (1)



However, even in a dried electrolyte (5 ppm H<sub>2</sub>O content), we still observe significant current response in this potential region ([Figure S1b](#)). Moreover, the reaction order analysis shown in [Figure S2](#) as log(*i*) vs log([H<sub>2</sub>O]) gives a reaction order of ~0.6. This is indicative of either multiple parallel reactions or of a multistep reaction taking place at the surface.

In order to further illuminate the nature of these reactions, we have probed the chemical composition of the porous film at the electrode surface by means of Fourier transform infrared (FTIR) spectroscopy and X-ray photoelectron spectroscopy (XPS). Snapshots of the surface film composition were taken at 5 different potentials: 2, 1.75, 1.5, 1.25, and 1 V. The evolution of FTIR and C 1s XPS spectra with increasingly negative potentials are shown in [Figure 1c,e](#), respectively. No detectable amount of any species was observed at or positive of 1.75 V consistent with no film formation observed in AFM images at 1.75 V. At 1.5 V several bands start to appear in the FTIR spectra and become increasingly stronger at 1.25 and 1.0 V. We first note the absence of strong vibrations around 1800 cm<sup>-1</sup>; the region with the most prominent vibrational modes of the EC/LiClO<sub>4</sub> solvate ([Figure S3](#)). This indicates that even with gentle washing of our samples (see [Methods](#) for details), we were able to remove most of the residual electrolyte from the sample surface and thus prevent any potential interference in the interpretation of the FTIR and XPS data. Next, we identified two sets of bands, which we attribute to two

compounds forming the solid film observed on the Au(111) surface. The two broad absorption peaks at 1524 and 1436 cm<sup>-1</sup>, and a sharp peak at 876 cm<sup>-1</sup> (red dashed lines in [Figure 1c](#)) give a close match with literature data<sup>33,34</sup> as well as the reference spectra of a Li<sub>2</sub>CO<sub>3</sub> thin film ([Figure S3](#)). The second set of bands (black dashed lines in [Figure 1c](#)) is assigned to a lithium alkyl carbonate R–CO<sub>3</sub>Li, with uniquely characteristic vibrational modes for this group of compounds at 1665 and 1318 cm<sup>-1</sup> that belong to O=C=O asymmetric stretching and CH<sub>2</sub> wagging. It is commonly accepted by the LiB community that the Li-alkyl carbonate obtained by electrochemical reduction of ethylene carbonate is LEDC.<sup>9,35,36</sup> More recently, however, this “common knowledge” has been disputed by Wang et al. in a rigorous study of complex interconversion equilibria between various R–CO<sub>3</sub>Li compounds in DMSO. Their study suggests that LEMC is the most likely component of the SEI.<sup>25</sup> We will return to the discussion of the exact chemical nature of the alkyl carbonate later in the article. At this point, we continue with the analysis of the surface film, with FTIR data pointing to Li<sub>2</sub>CO<sub>3</sub> and R–CO<sub>3</sub>Li as the main two constituents of our SEI on the Au(111) surface. This interpretation is further corroborated by XPS data, which show increased intensities of lithium carbonate and C–O functionalities at 290.0 and 286.5 eV, respectively, as the potential limit of the scan is decreased from 2 to 1 V ([Figure 1e](#)). These functional groups are further consistent with an alkyl carbonate or a mix of Li<sub>2</sub>CO<sub>3</sub> with alkyl carbonate. We also note that these are distinct from carbonate signals arising from the solvent, which are expected at higher binding energies of 291.0 eV as discussed further below. The appearance of the carbonates on the Au(111) surface exactly follows the current profile in the voltammogram, with significant amounts of carbonate(s) appearing only below 1.75 V.

Having previously established that the observed current in the 1.75–1 V potential range at least partially corresponds to water reduction, we were curious to see how the addition of water to the electrolyte affects the SEI formation. The AFM image in [Figure 1g](#) shows that a much thicker film of high porosity is formed. Furthermore, a change in morphology from granular to more fiber-like is observed. Surprisingly, the chemical composition of the film did not significantly change, still predominantly consisting of Li<sub>2</sub>CO<sub>3</sub> and R–CO<sub>3</sub>Li. However, having deposited much more material, all the signals previously observed in the FTIR and XPS spectra for the SEI formed in the “low water content” electrolyte, were significantly accentuated. No new species were detected by either technique, and no significant presence of LiOH was detected, as would have been expected in the case of amplified water reduction via [reaction 1](#).

Similarly, on other metal surfaces, the FTIR data in [Figure S4](#) reveal a SEI comprised predominantly of R–CO<sub>3</sub>Li and Li<sub>2</sub>CO<sub>3</sub>, which is observed exactly in the potential range of water electroreduction. Because the HER from water commences at different potentials on individual metals, a trend is observed that precisely matches the HER activity trend on these metals, i.e., Ir ~ Pt ≫ Au > Cu. This trend, which closely follows the work function of the pure metals, arises due to the necessity to establish a high enough coverage of Li<sup>+</sup> at the electrode surface. Li<sup>+</sup> stabilizes the activated complex [Li<sup>+</sup>–OH<sub>2</sub>–Li<sup>+</sup>], promoting the rate of [reaction 1](#). These results suggest that water is not only involved in the parallel reaction of H<sub>2</sub> and LiOH formation but is also actively participating in



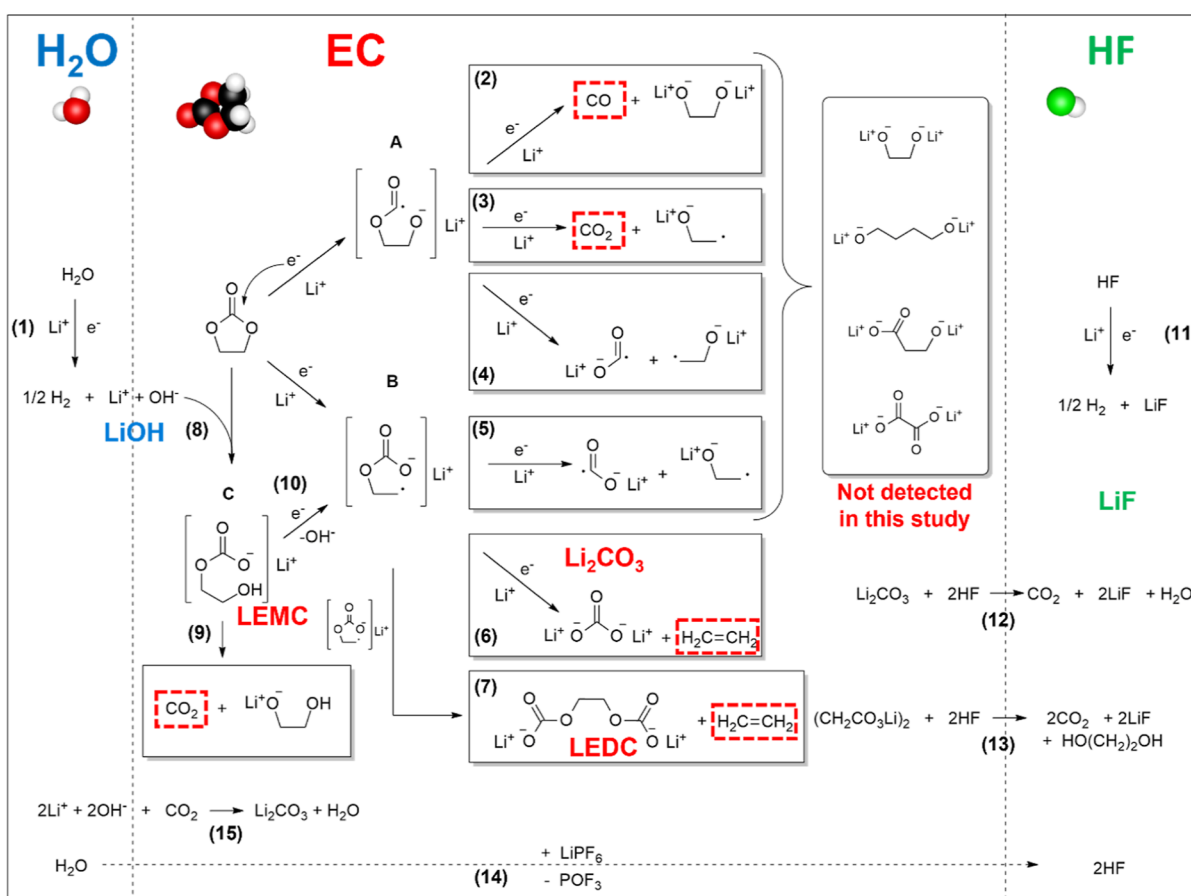


**Figure 2.** Possible reaction pathways for electrochemical reduction of EC with different intermediates and products. Paths A and B involve a first electrochemical step, followed by either a second electrochemical or a chemical step. An alternative path C is proposed involving a nucleophilic attack by  $\text{OH}^-$  on EC in the first step, followed by electrochemical reduction in the subsequent steps. Also shown are the electroreduction of  $\text{H}_2\text{O}$  and HF, as well as the reactions linking these three species and their respective (electro)chemistries.

the reactions producing the two main components of the SEI on the gold surface, i.e.,  $\text{R-CO}_3\text{Li}$  and  $\text{Li}_2\text{CO}_3$ .

With substantially more material at the surface, it becomes easier to interpret the FTIR and XPS spectra, as the peak intensities of the main SEI components increase while potential impurities stay in the “background”. Again, the bands associated with  $\text{Li}_2\text{CO}_3$  are clearly visible at  $1505\text{ cm}^{-1}$  (note that a small shift from  $1524\text{ cm}^{-1}$  is observed with thicker films) and  $1436$  and  $876\text{ cm}^{-1}$ , while the complete set of vibrational frequencies arising from  $\text{R-CO}_3\text{Li}$  can now be seen well discerned at  $1665$ ,  $1450$ ,  $1408$ ,  $1345$ ,  $1312$ ,  $1110$ ,  $1084^-$ , and  $829\text{ cm}^{-1}$  (Figure 1d; for detailed assignments of all the bands, see Figure S5 and Table S1). The latter set of absorption peaks is an exact match with the LEDC synthesized by Wang et al. in their recent study.<sup>25</sup> Moreover, the absence of characteristic strong vibration modes at  $1063$  and  $3383\text{ cm}^{-1}$ , which should be observed in compounds with  $\text{C-OH}$  functionality, suggests that the alkyl carbonate in our SEI is LEDC and not LEMC. The XPS data in Figure 1e further support this claim, with the  $\text{CO}_3$  vs  $\text{C-O}$  peak intensity ratio in favor of the carbonate group, consistent with a mixture of LEDC and  $\text{Li}_2\text{CO}_3$ .

Based on the abovementioned experimental evidence, we now turn to a possible reaction mechanism leading to the observed SEI composition. There are several possible routes for the electrochemical reduction of EC, involving multiple chemical and electrochemical steps. Most of them have been

well documented in the literature.<sup>13,37–39</sup> It seems that the first electron transfer creates a radical intermediate, which undergoes ring opening via two possible paths that are marked as path A and path B in Figure 2. This short-lived<sup>40</sup> intermediate can then undergo further chemical transformation or electron transfer, leading to a limited number of possible gaseous, soluble and insoluble products, including  $\text{CO}$ ,  $\text{CO}_2$ , ethylene, lithium glycolate, lithium oxalate,  $\text{Li}_2\text{CO}_3$ , and LEDC (see reactions (2–7) in Figure 2). By detecting evolved gases on the graphite anode during initial charge, Onuki et al. have shown that EC gets reduced by both paths A and B,<sup>37</sup> most likely due to the sterically open nature of the cyclic EC molecule. Our FTIR and XPS analyses of the SEI on metals clearly confirm the formation of  $\text{Li}_2\text{CO}_3$  and LEDC, presumably through path B in Figure 2. As explained later in the text, we were able to confirm Onuki’s findings on graphite powder samples, i.e., the EC reduction proceeds through both path A and B. Due to the low surface area of the metal samples, however, the evolved gases are below the detection limit of on-line electrochemical mass spectrometry (OEMS), at least in the low water content electrolyte. This changes in the presence of water, where  $\text{H}_2$  from reaction 1 and ethylene from reaction 6 can be detected on gold and platinum (Figure S11). Most importantly, however, none of the routes 1–6 provide any explanation for how water could be involved in the reaction mechanism and enhance the formation of  $\text{Li}_2\text{CO}_3$  and LEDC as observed experimentally. We therefore suggest a third

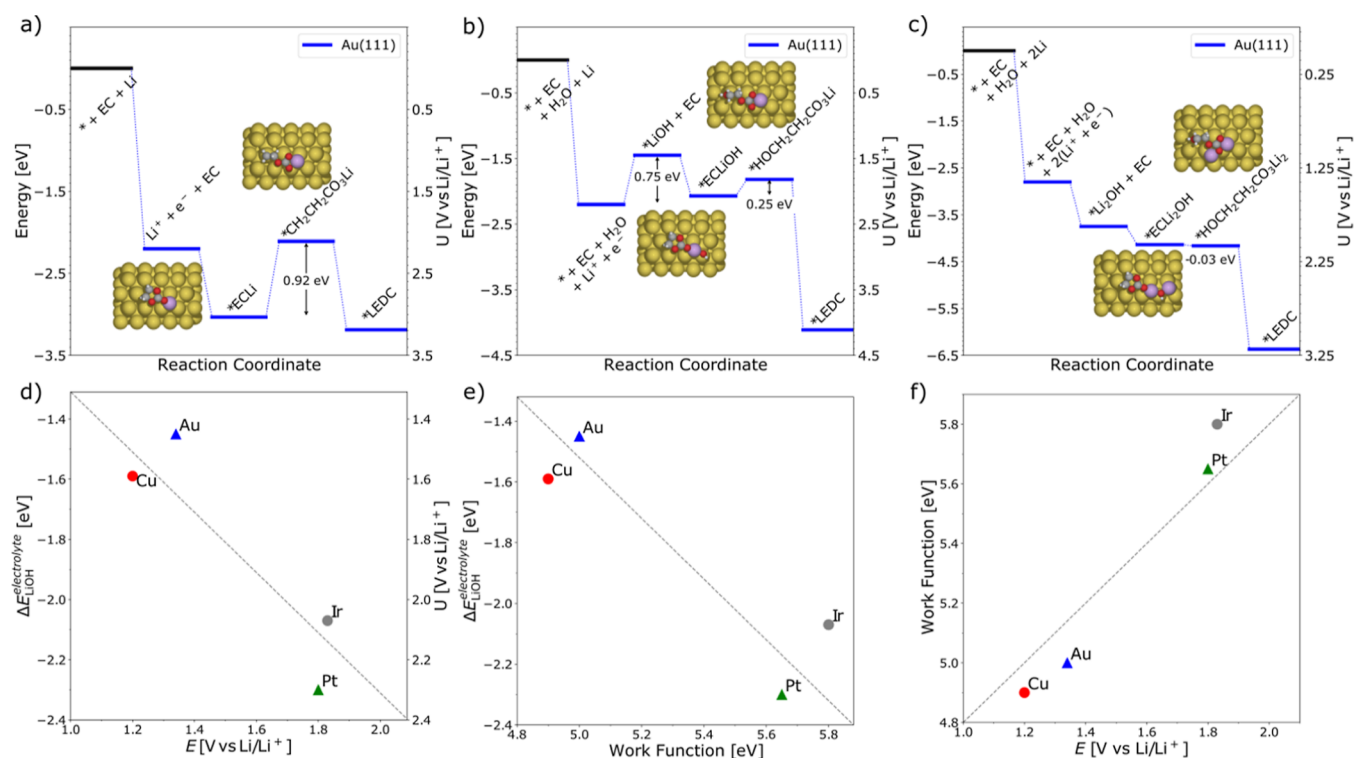


**Figure 3.** Energy diagram for EC reduction on Au(111) with different adsorbed species involved. (a) \*Li involved; (b) \*LiOH involved (note that the \*ECLiOH intermediate is LEMC); (c) \*Li<sub>2</sub>OH involved. Gold: Au(111); purple: Li; red: oxygen; gray: carbon; white: hydrogen. Correlations between (d): the experimental electrochemical response and the calculated adsorption energy of \*LiOH (calculated vs slab + electrolyte and Li bulk and H<sub>2</sub>O) and the calculated potential for having \*LiOH shown in the second y axis; (e) work function of the clean metal slabs and the calculated adsorption energy of \*LiOH; (f) experimental electrochemical response and the work function of the clean metal slabs.

possible path C, which begins via [reaction 8](#) with a nucleophilic attack of EC by  $\text{OH}^-$  generated from the electroreduction of water in [reaction 1](#)



Note that the “activated complex” in path C is actually LEMC, as suggested by Wang et al. In fact, this compound is not a reduced form of EC at all, as it is obtained by mere recombination of EC and LiOH. Assuming the fast formation of OH<sup>-</sup> in [reaction 1](#) and a rate determining reaction with EC in [reaction 8](#) would give a reaction order of 2/3 with respect to water, a plausible explanation for the observed value of 0.6. EC ring opening through OH<sup>-</sup> driven hydrolysis is well documented<sup>41</sup> and can lead to complete decomposition to CO<sub>2</sub> and glycolate through reaction 9 or enter an electrochemical reduction via reaction 10, producing the intermediate that leads to Li<sub>2</sub>CO<sub>3</sub> and LEDC.

In order to evaluate their relative favorability, we performed DFT calculations of the energetics of each path outlined in [Figure 2](#). We found that path B is more favorable than path A on all metals investigated ([Figure S12](#)). However, the EC ring-opening barrier observed in simulations following path B for metals cannot explain the catalytic EC reduction trends observed experimentally. Therefore, EC reduction in the presence of water was considered on the different metals as well. Following the H<sub>2</sub>O reduction trends investigated previously (see Section S3 in the [Supporting Information](#)), we probed the effect of three possible surface species on EC electroreduction: \*Li, \*LiOH, and \*Li<sub>2</sub>OH (where \* represents the metal active site). [Figure 3a–c](#) shows the free energy diagrams for EC reduction on Au(111) involving \*Li,

$^*\text{LiOH}$ , and  $^*\text{Li}_2\text{OH}$ , respectively. In Figure 3a, EC reduction (EC ring-opening following path B in Figure 2) shows a very high barrier (0.92 eV) for breaking the carbon–oxygen bond when only  $^*\text{Li}$  is involved. Figure 3b,c illustrates that the presence of  $\text{OH}^-$  from water reduction stabilizes the EC ring-opening structure, forming the LEMC ( $\text{HOCH}_2\text{CH}_2\text{CO}_3\text{Li}$ ) intermediate. From the LEMC intermediate the energy decreases toward LEDC as long as  $^*\text{LiOH}$  or  $^*\text{Li}_2\text{OH}$  species are present. Similar effects were observed for other metals, like Pt(111), Cu(111), and Ir(111), as shown in Figure S15. We note that  $^*\text{LiOH}$  is also involved in the HER from  $\text{H}_2\text{O}$  on metal surfaces (see Section S3 in the Supporting Information), indicating the connection between  $\text{H}_2\text{O}$  reduction and EC reduction. All the findings support that the presence of  $\text{H}_2\text{O}$  on all metal surfaces promotes LEDC formation from EC reduction. In addition, Figure 3d–f shows that the potential for the electrochemical response measured in experiments is correlated one-to-one with the adsorption energy of  $^*\text{LiOH}$  and thereby to the work function of the metal surfaces. This suggests that the experimentally observed activity trends for EC reduction ( $\text{Ir} \sim \text{Pt} \gg \text{Au} > \text{Cu}$ ) can be described by the work function of the metals, since it determines the adsorption energy of  $^*\text{LiOH}$ , which catalyzes EC reduction toward LEDC. Note that this does not preclude the reaction to still partially proceed through paths A and B as well. However, as seen from the reaction mechanisms and their energetics, it is unlikely that LEMC is stable on the electrode surface as it can either chemically decompose through reaction 9 or electrochemically transform via reaction 10.

## 2.2. Electrochemistry of H<sub>2</sub>O and EC on Model Carbon Systems.

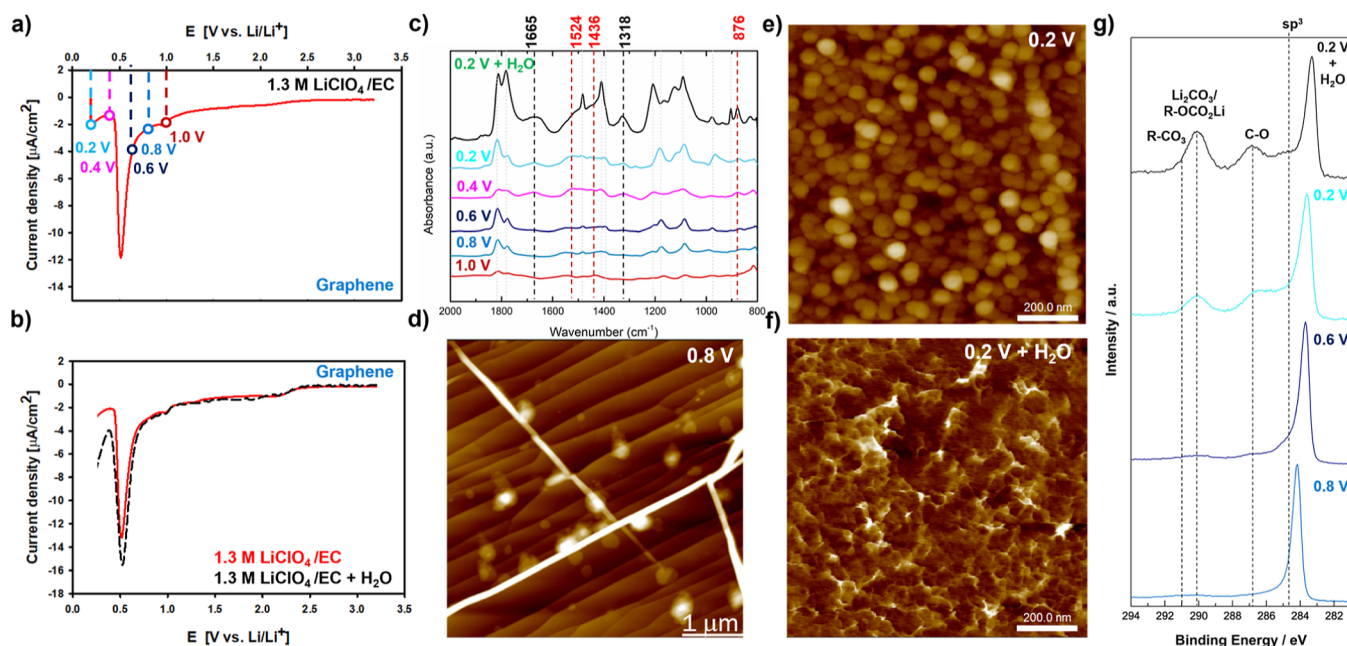


**Figure 4.** (a) Electrochemical response of low-defect-density graphene (LDG) in 1.3 M  $\text{LiClO}_4/\text{EC}$ ; first scan, taken at 1 mV/s in the negative direction. (b) Comparison of first potential scans from 3.2 to 0.2 V on LDG in 1.3 M  $\text{LiClO}_4$  with and without added water. A small but clearly visible increase in the signal can be seen. (c) Evolution of FTIR spectra with potential scans to different potentials—snapshots were taken at 1.0, 0.8, 0.6, 0.4, and 0.2 V vs  $\text{Li}/\text{Li}^+$ . The FTIR spectrum after the potential scan to 0.2 V in the electrolyte with 1000 ppm added water is also shown. (d) AFM image of the SEI formed on LDG after potential scan to 0.8 V in the “low water content” (<20 ppm)  $\text{LiClO}_4/\text{EC}$  electrolyte. (e) AFM image of the SEI formed on LDG after potential scan to 0.2 V in the “high water content” (1000 ppm)  $\text{LiClO}_4/\text{EC}$  electrolyte. A clear morphological change is visible. A more granular film is obtained in the “low water content” electrolyte, while a thicker, amorphous film can be found after the first scan in the “high water content” electrolyte. (f) AFM image of the SEI formed on LDG after potential scan to 0.2 V in the “low water content” (<20 ppm)  $\text{LiClO}_4/\text{EC}$  electrolyte. (g) C 1s XPS spectra of the LDG surface after potential scans to 0.8, 0.6, and 0.2 V. For comparison, the C 1s spectrum is also shown for the LDG surface after the potential scan to 0.2 V in the  $\text{LiClO}_4/\text{EC}$  electrolyte containing 1000 ppm of  $\text{H}_2\text{O}$ .

systems and real graphitic samples, we proceed to explore the  $\text{H}_2\text{O}$  and EC electrochemistries on model carbon systems, including epitaxially grown graphene with low surface defect density (LDG), and highly oriented pyrolytic graphite with either the basal or edge plane exposed to the electrolyte (b-HOPG and e-HOPG). These surfaces provided different degrees of complexity in terms of the amount of defects (mostly grain boundaries and steps) found on each, following the order  $\text{LDG} < \text{b-HOPG} \ll \text{e-HOPG}$ .

We first examine SEI formation on LDG samples. As shown by AFM imaging (Figure S7), LDG offers the closest possible approximation to a defect-free, well-ordered graphite surface, with large,  $\sim 10 \mu\text{m}$  grains separated by rare grain boundaries. Note that no significant Li intercalation is expected due to the predominant basal plane nature of this sample, providing a good opportunity to study SEI formation deconvoluted from lithium intercalation. The electrochemical response of LDG, as shown in Figure 4a, is dominated by a sharp reduction peak observed at 0.5 V in the negative sweep from 3.2 to 0.2 V. Unlike on the Au(111) surface, the graphene surface is almost completely passivated after the first sweep. AFM imaging of the surface after the first sweep confirms that a denser, more compact SEI is found on the surface (Figure 4f). The same analysis protocol as in the case of metal samples is employed for the graphene sample, with snapshots of the surface film composition taken at 5 different potentials: 1, 0.8, 0.6, 0.4, and 0.2 V. In contrast to the Au(111) surface, we first notice that, in addition to the two familiar sets of bands described below, the FTIR spectra reveal a third set of vibrations at 1864, 1798, 1481, 1392, 1160, 1070 $^-$ , and 971  $\text{cm}^{-1}$  that starts appearing

at much more positive potentials, around 1 V. These belong to the  $\text{EC}/\text{Li}^+$  solvate (see comparison with reference spectra in Figure S6). Interestingly, these bands do not disappear even with extensive washing and are certainly not coming from the SEI on the graphene surface. Instead, our AFM image in Figure 4d clearly shows the formation of bright pockets mostly around grain boundaries/defects. These bubble-like structures have been reported before on the basal HOPG surface in several studies<sup>42–44</sup> and are thought to belong to the  $\text{Li}^+/\text{EC}$  solvate, trapped between the graphene layers. This is confirmed by our FTIR results. The solvate bands disappear from the FTIR spectra after exposure to UHV, consistent with evacuation of the solvent from the graphene multi-layer host and with the XPS spectra that show no significant solvent presence at any potential. As seen from the evolution of the FTIR spectra, solvate intercalation into the graphene structure depends on potential; however, only a tiny charge is passed between 1.0 and 0.8 V, while a significant intercalation of the solvated  $\text{Li}^+$  is observed. This seems to suggest that intercalation precedes the charge transfer, but a more detailed discussion of this phenomenon is beyond the scope of this paper. The main SEI formation process starts just negative of 0.6 V with the appearance of absorption peaks at 1524, 1436 $^-$ , and 876  $\text{cm}^{-1}$  that belong to  $\text{Li}_2\text{CO}_3$  and the signature vibrational modes at 1667 and 1318  $\text{cm}^{-1}$  that belong to LEDC. Note that other LEDC peaks are somewhat obscured due to overlap with the solvent absorption bands. Nonetheless, the formation of LEDC/ $\text{LiCO}_3$  is further confirmed by the C 1s XPS spectra (Figure 4g), which show the evolution of peaks at 290.0 and 286.5 eV just negative of 0.6 V, where we also start observing



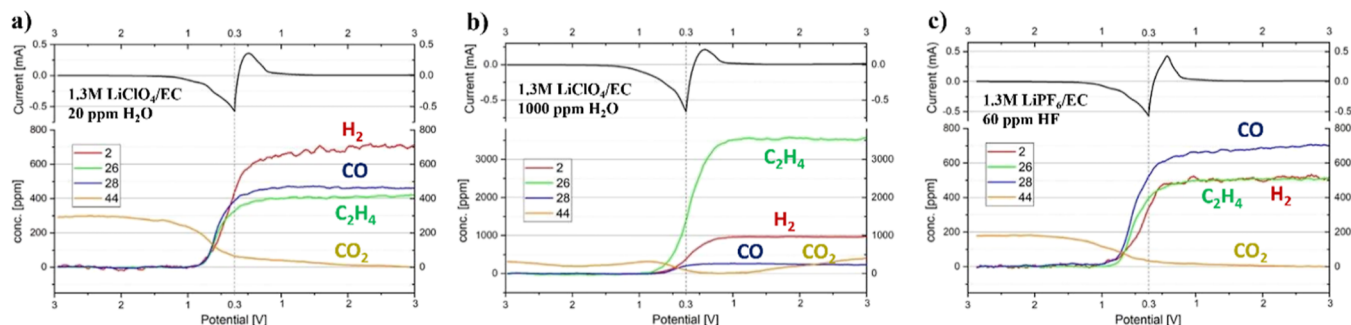


**Figure 5.** OEMS measurements of gas evolution from SMG-A5 graphite electrodes during the potential scan 3.0–0 V vs Li/Li<sup>+</sup> in three electrolytes. (a) 1.3 M LiClO<sub>4</sub>/EC with 20 ppm of H<sub>2</sub>O. (b) 1.3 M LiClO<sub>4</sub>/EC with 1000 ppm of H<sub>2</sub>O and (c) 1.3 M LiPF<sub>6</sub>/EC with 60 ppm of HF. H<sub>2</sub> ( $m/z = 2$ ), ethylene C<sub>2</sub>H<sub>4</sub> ( $m/z = 26$ ), CO ( $m/z = 28$ ), and CO<sub>2</sub> ( $m/z = 44$ ) signals were followed. The potential scan was done with 0.2 mV/s.

significant currents in the voltammogram. As stated previously, these features belong to CO<sub>3</sub> and C–O functionalities, respectively. We conclude, therefore, that the electrochemistry of EC reduction is the same on graphene as it is on metals, albeit displaced by ~1 V toward more negative potentials, resulting in roughly similar SEI compositions, but with somewhat different morphologies.

In analogy to the experiments mentioned above on metals, we observe increases both in the reduction peak currents and the SEI thickness upon addition of 1000 ppm of water to the electrolyte (AFM in Figure 4f). Again, significant differences in morphology are observed, with the film displaying more fabric-like properties. Both Li<sub>2</sub>CO<sub>3</sub> and LEDC signals in FTIR and XPS C 1s spectra also increase, confirming that the proposed reaction scheme on metals (Figure 2) translates to these carbon systems as well. The main difference, however, is in the extent of the promoting effect that the same concentration of water has on graphene substrates. On Au(111), the increase in the reduction current is multiple times higher than that on LDG. Similarly, a higher amplification of the LEDC and Li<sub>2</sub>CO<sub>3</sub> signals in FTIR spectra is observed on gold compared to graphene, which can be linked to the amount of the two compounds produced during the potential sweep. It follows, that the graphene surface falls exactly on the same trend line as all the metals, i.e., the higher the work function of the electrode material, the more positive the adsorption potential of Li<sup>+</sup> onto the surface and the more positive the reduction potential of EC and H<sub>2</sub>O. In addition, the better the catalytic ability of the surface for H<sub>2</sub>O reduction, the more pronounced is the enhancement of LEDC and Li<sub>2</sub>CO<sub>3</sub> contents in the SEI through path C in our reaction scheme.

To conclude the section on model carbon systems, we briefly look at the basal and edge plane HOPG. In addition to grain boundaries, these surfaces also contain a significant density of steps. A lot has been published on these two systems,<sup>20,23,26,27,42–47</sup> so we just summarize our main observations here. As can be seen from Figure S8, the electrochemical response on basal HOPG depends on the quality of HOPG and the quality of individual cleavage, always displaying a peak at 0.5 V, but often showing additional peaks at 0.7 and 0.8 V. As shown in the accompanying AFM images, these two additional features appear on HOPG surfaces with more defects. As in the case of the LDG, we can see an extensive solvate intercalation has already taken place before any significant currents. In the case of HOPG, the EC/Li<sup>+</sup> co-intercalation is so extensive that it is now visible even with XPS (in spite of removal of a significant portion of the solvent in

UHV). Typical EC R–CO<sub>3</sub> functionality is observed at ~1 eV higher binding energy compared to LEDC and Li<sub>2</sub>CO<sub>3</sub>, i.e., at 291.0 eV. At 0.8 V, the HOPG terraces still look pristine. As we move toward more negative potentials, we eventually see the reaction commence at steps/defects and finally at terraces at 0.5 V. AFM images at 0.2 V clearly show complete coverage of the terraces, while XPS data confirm the LEDC/Li<sub>2</sub>CO<sub>3</sub> composition of the SEI. Finally, we look at the edge HOPG surface. Here, the massive current observed between 1.0 and 0.2 V belongs to lithium intercalation. Note that the processes of solvate intercalation as well as SEI formation, which is represented only by a tiny current, are superimposed on the Li-intercalation, making the deconvolution of individual processes practically impossible. This is part of the reason why SEI studies on real systems are plagued by so many interferences and ambiguous outcomes.

### 2.3. Electrochemistry of H<sub>2</sub>O and EC in Real Systems.

To complete the investigation of the H<sub>2</sub>O-EC electrochemistry, we monitored the SEI formation on real, high-surface-area graphitic samples. As mentioned above, we believe that FTIR, XPS, and electrochemical data on these complex samples can often give misleading results due to interference from the EC/Li<sup>+</sup> solvate within the graphite structure as well as the trapped electrolyte in the SEI and chemicals used in the preparation of the graphite composite electrodes. OEMS, however, enables quantitative monitoring of evolved gases during the SEI formation during the potential scan, while avoiding most of the interferences encountered in other techniques. In Figure 5, we summarize the gas evolution data during the first potential scan in the SMG-A5 graphite/Li cell. Because of the 100–500 times higher surface area of the graphite electrode compared to metal mesh or crystal electrodes, gas evolution during SEI formation is much more apparent compared to the metal mesh electrodes. Several observations are noteworthy: In LiClO<sub>4</sub>/EC electrolyte with low water content, we detected three gases—namely H<sub>2</sub>, CO, and ethylene (C<sub>2</sub>H<sub>4</sub>)—that start evolving at roughly 0.75 V (Figure 5a). Considering the high number of defects in the graphite powder, this potential correlates well with the potential where we first observe the formation of the SEI on basal and edge HOPG. While hydrogen is produced through water reduction via reaction 1, CO and C<sub>2</sub>H<sub>4</sub> are formed in the “EC cycle” in reactions 2, 6, and 7 through path A and B (see reaction scheme in Figure 2), together with (CH<sub>2</sub>Oli)<sub>2</sub>, Li<sub>2</sub>CO<sub>3</sub>, and LEDC. Note that roughly equal amounts of CO and C<sub>2</sub>H<sub>4</sub> (460 and 420 ppm, respectively) are produced in the first charging cycle in the low-water-content electrolyte. This

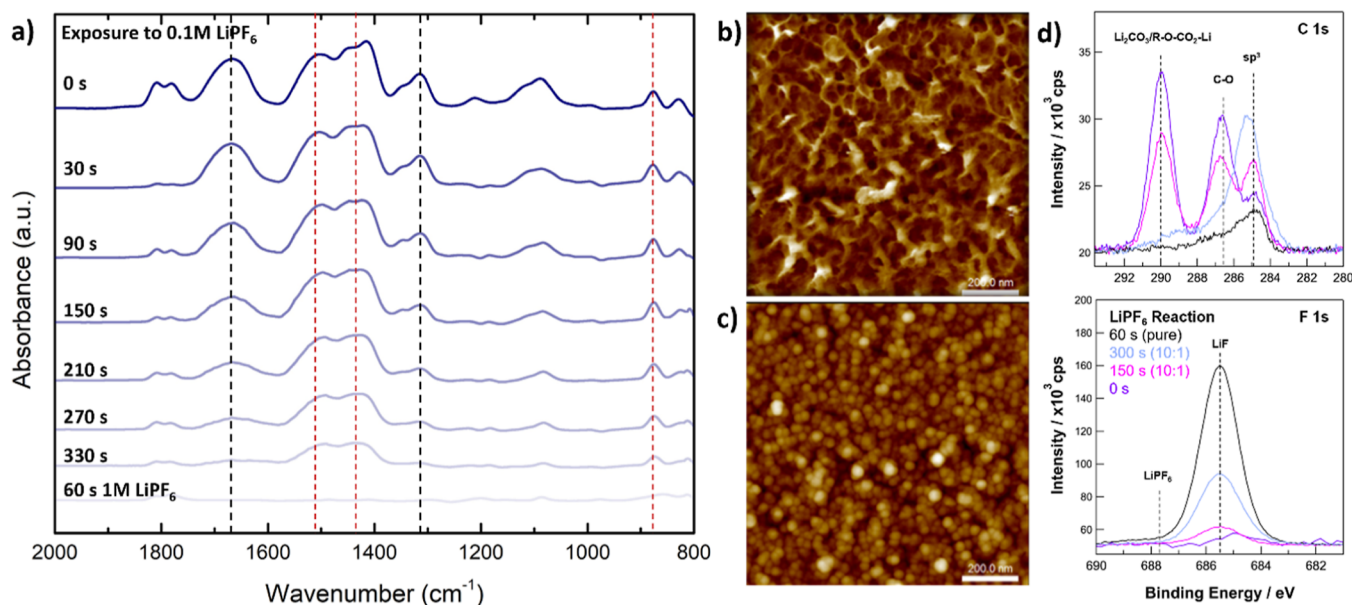


**Figure 6.** (a) Evolution of FTIR spectra with time after exposing the SEI ( $\text{LEDC}/\text{Li}_2\text{CO}_3$ ), obtained in  $\text{LiClO}_4$  electrolyte, to undiluted or 10 $\times$  diluted 1 M  $\text{LiPF}_6$  (HF concentration 80 and 8 ppm, respectively) (b) AFM image of the  $\text{LEDC}/\text{Li}_2\text{CO}_3$  SEI before exposure to  $\text{LiPF}_6$  (c) AFM image of the SEI after exposure to  $\text{LiPF}_6$ ; a clear morphological change has taken place in addition to the chemical transformation (d) XPS C 1s and F 1s show the disappearance of  $\text{LEDC}/\text{Li}_2\text{CO}_3$  and appearance of  $\text{LiF}$  relatively quickly after bringing the SEI in contact with  $\text{LiPF}_6$ . Note that the black curves in the C 1s and F 1s are charge referenced differently due to differential charging of the highly insulating  $\text{LiF}$  layer (see the main text and Supporting Information for additional discussion).

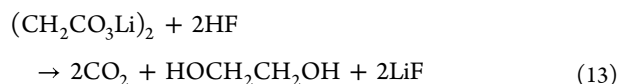
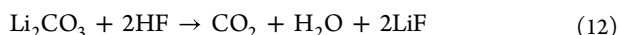
suggests that the energetics of path A and B for this system are roughly the same. Interestingly, we also observe changes in the concentration of  $\text{CO}_2$ , which is inherently present in this electrolyte and is found in the headspace (200–300 ppm) at open circuit voltage (OCV). Upon polarization,  $\text{CO}_2$  is consumed at around 0.75 V, where the other gases are formed. We suggest that the most likely reaction responsible for the consumption of this native  $\text{CO}_2$  is reaction 15, formation of  $\text{Li}_2\text{CO}_3$  through neutralization of  $\text{CO}_2$  with  $\text{OH}^-$ , which is formed through the reduction of water in reaction 1. Most importantly, in the high-water-content electrolyte a nine-fold increase in ethylene production is detected, while CO formation is cut in half (Figure 5b). This result complements the results obtained on model metal and carbon systems, which display a 5–10-fold increase of LEDC formation in the presence of 1000 ppm of water via reaction 6 as a coproduct of  $\text{C}_2\text{H}_4$ . Furthermore, it confirms the relationship between the water and EC reaction paths. As proposed above,  $\text{OH}^-$  created by water reduction acts as a catalyst for reaction 6 by providing an energetically more favorable path C. While the initial amount of  $\text{OH}^-$  is “buffered” by inherent  $\text{CO}_2$ , the excess is available to form intermediate LEMC, which either decomposes into  $\text{CO}_2$  and glycolate or is electrochemically transformed into LEDC and  $\text{C}_2\text{H}_4$ . This results in the observation of two opposite trends regarding  $\text{CO}_2$  concentration, with an initial decrease followed by gradual and steady concentration increase. Finally, in Figure 5c, we show the gas evolution from a  $\text{LiPF}_6/\text{EC}$  electrolyte. One of the characteristics of this electrolyte is the very low content of water, due to its quantitative reaction with  $\text{PF}_6^-$  to form  $\text{HF}$ <sup>31,48,49</sup> via reaction 14 in the reaction scheme in Figure 2. Therefore, as in the case of low-water-content  $\text{LiClO}_4/\text{EC}$  electrolyte, the contribution of reaction path C to the overall product formation is significantly diminished, while the formation of CO through path A is favored. It seems that the  $\text{CO}/\text{C}_2\text{H}_4$

ratio, which is indicative of the representation of individual reaction paths in the overall reaction mechanism, is linked to the acidity of the electrolyte. In the most acidic electrolyte (HF containing  $\text{LiPF}_6/\text{EC}$ ), the ratio is the highest, suggesting the preference for path A, while the most alkaline electrolyte (high water content  $\text{LiClO}_4/\text{EC}$ ) favors path C.

In general, on all the systems investigated in the study, we find that the (electro)chemistry closely follows the same reaction mechanism. In disagreement with some previous reports,<sup>47</sup> we clearly show the electrocatalytic nature of the SEI formation, as well as a clear link between model and real systems.

**2.4. Interaction of HF,  $\text{H}_2\text{O}$ , and EC Electrochemical Cycles in Li-Ion Battery Electrolytes.** Considering that most commercial Li-ion battery electrolytes are based on  $\text{LiPF}_6$  mixtures with cyclic and linear organic carbonates, it makes sense to establish a link between our findings in  $\text{LiClO}_4$  electrolyte in this study and more commonly used LIB electrolytes. In our previous study, we have followed the formation of HF from water impurities and its electrocatalytic transformation to  $\text{H}_2$  and  $\text{LiF}$  in  $\text{LiPF}_6$ -based electrolytes.<sup>31</sup> By exposing the SEI made in  $\text{LiClO}_4$  to HF-containing  $\text{LiPF}_6$ , we now link the HF, EC, and  $\text{H}_2\text{O}$  reaction paths together. We notice that in 1.3 M  $\text{LiPF}_6/\text{EC}$  electrolyte, both carbonates are no longer detectable with FTIR after 60 s. In order to follow a slower evolution of the FTIR and XPS signals of the SEI, we diluted the  $\text{LiPF}_6/\text{EC}$  electrolyte with  $\text{LiClO}_4/\text{EC}$  electrolyte in a 1:10 ratio. Figure 6a shows the gradual decrease in LEDC and  $\text{Li}_2\text{CO}_3$  vibrational modes upon exposure of the SEI on Au(111) surfaces to  $\text{LiPF}_6$ -containing electrolyte. Even after 5 min, the AFM images (Figure 6c) still show the presence of a film on the surface, albeit with a different morphology. As determined by XPS (Figure 6d), this film is pure  $\text{LiF}$ , in agreement with our report on SEI composition in  $\text{LiPF}_6$  electrolytes generated in a flooded cell. Most significantly, no

carbonates are detected by XPS. Note that, for clarity, the black curves in Figure 6d are charge referenced differently from one another, even though they are from the same dataset, due to significant differential charging when a thick, highly insulating LiF layer is formed on the electrode surface. This phenomenon has been observed previously, and a detailed discussion about charge referencing of these complex surfaces is provided in the Supporting Information for the interested reader. These results suggest that, upon exposure to a sufficient amount of HF, both LEDC and  $\text{Li}_2\text{CO}_3$  are quantitatively transformed into LiF via reactions 12 and 13.



At the electrode/electrolyte interface, which is represented by the triangle in Figure 7, each of the three components, i.e.,

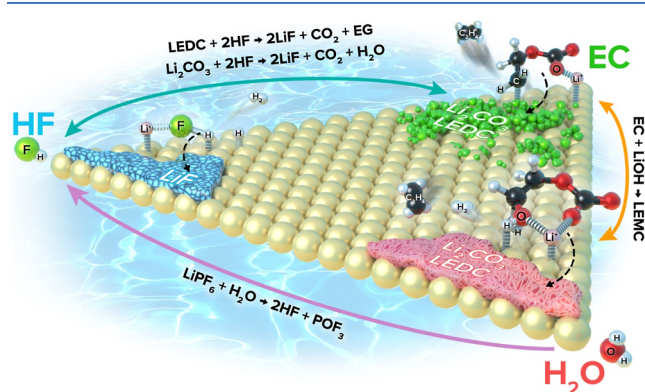


**Figure 7.** Schematic representation of three dominant SEI forming species in Li-ion battery electrolytes, i.e., EC, HF, and  $\text{H}_2\text{O}$ . As shown by DFT calculations, the presence of adsorbed  $\text{Li}^+$  plays the key role in electrocatalytic reduction of these three compounds. We show that water plays a catalytic role in EC electrochemistry, effectively reducing the energy barrier for the formation of LEDC and  $\text{Li}_2\text{CO}_3$ . Moreover, each of the chemistries involved in SEI formation also comes with a distinct morphology. Finally, the three molecules and their products are linked through chemical reactions taking place at the surface of the electrode as well as in the bulk of the electrolyte, which manifests itself through the complexity of the SEI composition.

HF,  $\text{H}_2\text{O}$ , and EC (shown in the corners of the triangle), undergoes its own electrochemical transformation. A delicate balance exists between the chemistries of the three major players/electrolyte components and, for the most part, determines the composition and morphology of the SEI. In this and our previous two studies, we demonstrated that all three electrochemical reactions are electrocatalytic in nature, an important fact that has often been overlooked. Consequently, these reactions take place at vastly different potentials depending on the electrode material or different surface sites on the same material (e.g., terraces, steps, or point defects). The overall electrochemistry for these reactions, however, does not change from system to system, which allows the results in model systems to be transferred to understand the behavior of real materials. Model systems are, by default, closer to the ideal systems used in computational efforts, such as DFT, which brings experiments closer to theory. Our studies of these three reactions show that the electrocatalytic nature of

these reactions stems from the potential-dependent structure of the double layer as well as the more typical interaction of the reactants with the electrode surface in the bond breaking and bond making processes. Specifically, the adsorption of  $\text{Li}^+$  onto the electrode surface, which allows the formation of energetically favorable activated complexes, is related to the work function of the electrode material, establishing a 2 V potential window between the most active Ir and the least active graphene surface. From a phenomenological point of view, this is a unique manifestation of the potential in electrocatalysis.

The complexity of the SEI formation and composition, however, does not end with the three electrocatalytic reactions described above. These electrochemical reactions are connected in a closed cycle by chemical reactions that take place at the interface or in the bulk of the electrolyte as shown on the sides of the triangle in Figure 7. Water in the bulk of the electrolyte enters the chemical reaction with  $\text{LiPF}_6$  to form HF (reaction 14). HF from the bulk of the electrolyte attacks LEDC and  $\text{Li}_2\text{CO}_3$  in the SEI and transforms them into LiF (reactions 12 and 13). Finally, LiOH, the product of electroreduction of  $\text{H}_2\text{O}$ , serves as a catalyst for the electrochemical formation of LEDC and  $\text{Li}_2\text{CO}_3$  (reactions 8 and 10), which has been shown for the first time in this study. We note that other reactions are possible and have been reported in the literature, but their products are either soluble, and hence not present in the SEI, or are just not as abundant as the main components described above, at least under the conditions investigated in this study. The composition of the SEI therefore depends predominantly on the balance between the (electro)chemistry of EC, water, and HF. This balance is heavily influenced by the experimental conditions used in a particular study, leading to vastly different outcomes, i.e., SEI compositions, reported in the literature, even in the same electrolyte. While our study does not directly address the relationship between the SEI composition and cell performance, it gives us a blueprint of how to create SEIs of any composition and morphology and thus link it to the cell performance in the future. We believe that our findings, while addressing important problems relevant for LiBs, point to much broader electrochemical phenomena that are of general importance for our fundamental understanding of electrochemical interfaces.

### 3. METHODS

**3.1. Extended Surface Electrode Preparation and Electrochemical Measurement.** Pt(111), Ir(111), Au(111), and Cu(111) electrode surfaces having  $\sim 0.283 \text{ cm}^2$  geometric area (discs of 6 mm diameter and 4 mm length, Princeton Scientific Corp.) were prepared by inductive heating (EASY-Heat, Ambrell) for 7 min at 1323 K for Pt, 5 min at 1073 K for Au and Cu, and 10 min at 1473 K for Ir in an controlled atmosphere (97% Ar/3%  $\text{H}_2$  gas mixture, Airgas). The crystal discs were slowly cooled down (ca. 7 min) to laboratory temperature ( $\sim 294 \text{ K}$ ) under the same atmospheric condition. The electrode surface was protected by a water droplet before being exposed to the laboratory atmosphere, and then carefully assembled into a rotating disk electrode (RDE) configuration (a polypropylene thin sheet was used to support the electrode disc during the RDE assembling, with the electrode surface facing toward the sheet protected by a thin water film). After the electrode was assembled, the RDE (the electrode surface always protected by a water droplet) was transferred into a glove box ( $<0.80$  ppm of oxygen gas,  $<0.5$  ppm of moisture). It



was first placed in the antechamber to let the water droplet dry completely under vacuum before being transferred into the glovebox's main compartment. Electrochemical measurements were performed inside the glovebox using a three-electrode glass electrochemical cell. Au wire was used as the counter electrode, separated from the working electrode compartment by a frit. Freshly exposed Li metal was used as the Li/Li<sup>+</sup> reference electrode. The working electrode surface was immersed into the electrolyte at controlled potential (3.2 V). All potentials are given vs Li/Li<sup>+</sup>. All measurements were controlled using a potentiostat (PGSTAT 302N, Metrohm Autolab). Electrochemical measurements were done with a scan rate of 1 mV/s starting in the negative direction. Although assembled in the RDE configuration, no rotation was used during the electrochemical measurements.

**3.2. Preparation of Carbon Samples.** Epitaxially grown graphene with low surface defect concentration (LDG) was grown on Pt(111) heated to 1473 K in methane flow by chemical vapor deposition.

The HOPG ZYA type crystal with a basal exposed plane (Princeton Scientific Corp.) was assembled into the RDE and freshly cleaved with adhesive tape inside the glove box prior to each experiment. The HOPG ZYA type crystal with an edge-exposed plane (Princeton Scientific Corp.) was cut parallel to the edge surface with a stainless-steel blade to expose a fresh surface and subsequently washed with THF, dried, and inserted into the RDE.

**3.3. Chemicals.** 1.3 M LiClO<sub>4</sub>/EC and 1 M LiPF<sub>6</sub>/EC were prepared from EC (Gotting), LiClO<sub>4</sub> (Battery grade, Sigma-Aldrich), and LiPF<sub>6</sub> (BASF). Tetrahydrofuran (THF, Sigma-Aldrich) was used for rinsing the electrodes after electrochemical measurements.

**3.4. Water determination.** Water content in electrolytes was measured using the Karl Fischer titration system (Metler-Toledo) placed inside an Ar-filled glovebox with the H<sub>2</sub>O level below 0.5 ppm.

**3.5. FTIR Measurements.** Fourier-transform infrared spectroscopy (FTIR) was used to probe the species present at the electrode surface after SEI formation. We utilized ex situ grazing angle external reflectance FTIR (Thermo-Fisher Nicolet iS50 with Pike Technologies VeeMax III accessory) at a 65° incidence angle (most sensitive to the surface species) with p-type polarized light (ZnSe polarizer positioned at the incident beam). After electrochemical SEI formation, the electrode was carefully rinsed with THF to remove any electrolyte residue (without compromising the SEI) and sealed in a glass jar prior to transferring to the FTIR instrument inside a glovebox. After transfer, the glass jar was opened, and the electrode surface was positioned in a way that guarantees the direct reflection of infrared light into the detector. The MCT detector (with a spectral resolution of 2 cm<sup>-1</sup>) of the FTIR instrument was cooled with liquid argon to provide enough sensitivity for detection of surface species. The electrode surface prior to electrochemical cycling served as the baseline for absorbance determination. Band assignment was performed with assistance of established literature.<sup>9,25,33–36</sup>

**3.6. AFM Measurements.** The AFM measurements were performed on a Bruker Dimension Icon AFM at tapping mode with a silicon cantilever (RFESPA-75, Bruker). The experiments were conducted in a vibrational isolation enclosure for imaging. All images were taken with a scan rate of 0.6 Hz, and scan sizes of 1 and 5 μm. After the images were acquired, the Nanoscope Analysis software was used to process the images.

Prior to the AFM measurements, all samples (electrode surfaces) were rinsed with THF to remove any residual electrolyte.

**3.7. XPS Measurements.** XPS measurements were performed using a Specs PHOIBOS 150 hemispherical energy analyzer using a monochromated Al Kα X-ray source. The load-lock of the analytical UHV system is connected directly to an Ar-filled glove box, enabling the loading of samples without any exposure to the ambient atmosphere. Survey spectra were measured using a pass energy of 40 eV at a resolution of 0.2 eV/step and a total integration time of 0.2 s/point. Core level spectra were measured using a pass energy of 20 eV at a resolution of 0.05 eV/step and a total integration time of 0.5 s/point. A charge neutralizing electron flood gun was used for some samples to attempt to address differential charging between highly insulating LiF and conductive substrates. Deconvolution was performed using CasaXPS software with a Shirley-type background and 70–30 Gaussian–Lorentzian peak shapes. Differential charging of SEI layers relative to the conductive substrates required different strategies depending on the substrate and SEI chemistries. Au(111) samples cycled in 1.3 M LiClO<sub>4</sub>/EC electrolytes and reacted with LiPF<sub>6</sub> electrolytes were primarily charge referenced using sp<sup>3</sup> carbon in the C 1s at 284.8 eV. Au(111) samples with higher amounts of LiF exhibited differential charging that was not easily corrected using charge neutralization, requiring an alternative charge referencing strategy using the position of sp<sup>3</sup> carbon for C 1s data and LiF (685.5 eV in the F 1s) for the F 1s data. Pristine HOPG samples used the position of graphitic carbon at 284.0 eV, while cycled graphene/HOPG samples used the position of Li carbonates in the Li 1s at 55.4 eV (consistent with the position measured on Au(111) samples) to control for differential charging as a function of SEI thickness. See the Supporting Information for a more detailed discussion of charge referencing, differential charging, and charge compensation on these samples.

**3.8. OEMS Measurements.** OEMS experiments were performed in an all PEEK OEMS cell similar to the cell developed by TU Munich.<sup>50</sup> Lithium foil (99.9% purity, Albemarle) was used as the counter electrode (CE) and two glass fiber discs (VWR, 205 μm thickness, 15 mm diameter) were used as the separator. The working electrode (WE) was placed on the separator and 1 mL of electrolyte was put on the electrode; the electric contact for the WE was made with a Pt wire (99.99% purity, Goodfellow, 0.1 mm diameter). The PEEK cell design allows for experiments without contact of the electrolyte with stainless steel.

All pieces of cell hardware were dried for at least 12 h at 60 °C under vacuum before usage. The glass fiber separators were dried for 5 h at 300 °C under vacuum in a glass oven (Buchi, Switzerland).

The graphite electrodes for the OEMS measurements consisted of 97 wt % SMG-A5 graphite powder (Hitachi), 1.5 wt % carboxymethyl cellulose binder (CMC Sunrose MAC200, NPI, Japan), and 1.5 wt % styrene-butadiene rubber binder (SBR, Zeon, Japan). The materials were mixed in a planetary orbital mixer (Thinky, USA) at 2000 rpm and 50 mbar for 10 min. The resulting ink was blade-coated onto a 20 μm thick, porous Celgard separator (H2013, Celgard, USA) at a wet-film thickness of 50 μm using an automatic coater (RK Print, UK).

This configuration allows for a reasonably short diffusion time for gases produced by the graphite electrode to the flow-

restricting capillary (on the order of several minutes), which connects the OEMS cell with the mass spectrometer, which is a requirement for measurements with the OEMS system.<sup>50</sup>

After assembling the cell and attaching the cell to the OEMS system, the cell was purged with argon and subsequently kept at open circuit voltage (OCV) for 4 h in order to obtain stable OEMS background signals. After this, a potential scan from OCV to 0.3 V vs Li/Li<sup>+</sup> followed by a scan to 3.0 V vs Li/Li<sup>+</sup> was performed with a scan rate of 0.2 mV/s. All potentials shown are referenced vs Li/Li<sup>+</sup> CE. To quantify the amount of evolved gases, the ion currents at different *m/z* values (*I<sub>z</sub>*) were normalized by the signal for the <sup>36</sup>Ar isotope and calibrated with calibration gases containing 2000 ppm of CO, C<sub>2</sub>H<sub>4</sub>, and H<sub>2</sub> in pure argon (further details can be found in Metzger et al.<sup>51</sup>).

**3.9. DFT Calculations.** The calculations are performed using the GPAW code.<sup>52,53</sup> The ASE package<sup>54</sup> has been used to handle the crystal structures. The calculations are performed using the revised Perdew–Burke–Ernzerhof (RPBE) functional<sup>55</sup> as the exchange–correlation functional. The calculations for these intermediates' adsorption energies are performed using a 5 × 4 × 3 unit cell with the last bottom layer kept frozen to reproduce the bulk of the slab and the two top layers let free to relax as well as the adsorbate. We use a 3 × 3 × 1 Monkhorst–Pack *k*-point (Gamma) grid and the wave functions were represented on a uniform real-spaced grid with 0.18 Å grid-spacing. A vacuum of minimum 10 Å on the *z* direction was employed. (For more details see the [Supporting Information](#)).

## ■ ASSOCIATED CONTENT

### Data Availability Statement

All data are available from the authors upon reasonable request.

### SI Supporting Information

The Supporting Information is available free of charge at <https://pubs.acs.org/doi/10.1021/acscatal.3c01531>.

Additional electrochemical, FTIR, OEMS, and AFM data on Au(111), Pt(111), Cu(111), Ir(111), and HOPG, reference FTIR spectra and detailed peak assignments for analytes of the SEI on Au(111), detailed description of XPS experiments including explanation of the applied charge referencing, and detailed description of computational modeling ([PDF](#))

## ■ AUTHOR INFORMATION

### Corresponding Author

**Dusan Strmcnik** – Materials Science Division, Argonne National Laboratory, Argonne, Illinois 60439, United States; National Institute of Chemistry, SI-1000 Ljubljana, Slovenia; [orcid.org/0000-0002-3021-2771](https://orcid.org/0000-0002-3021-2771); Email: [dusan.strmcnik@ki.si](mailto:dusan.strmcnik@ki.si)

### Authors

**Milena Martins** – Materials Science Division, Argonne National Laboratory, Argonne, Illinois 60439, United States; National Institute of Chemistry, SI-1000 Ljubljana, Slovenia  
**Dominik Haering** – Materials Science Division, Argonne National Laboratory, Argonne, Illinois 60439, United States; Department of Chemical and Biomolecular Engineering, Horiba Institute for Mobility and Connectivity, University of California Irvine, Irvine, California 92697, United States

**Justin G. Connell** – Materials Science Division, Argonne National Laboratory, Argonne, Illinois 60439, United States; [orcid.org/0000-0002-2979-2131](https://orcid.org/0000-0002-2979-2131)

**Hao Wan** – Nano-Science Center, Department of Chemistry, University of Copenhagen, DK-2100 Copenhagen, Denmark

**Katrine L. Svane** – Department of Energy Conversion and Storage, Technical University of Denmark, DK-2800 Kgs. Lyngby, Denmark

**Bostjan Genorio** – Faculty of Chemistry and Chemical Technology, University of Ljubljana, SI-1000 Ljubljana, Slovenia; [orcid.org/0000-0002-0714-3472](https://orcid.org/0000-0002-0714-3472)

**Pedro Farinazzo Bergamo Dias Martins** – Materials Science Division, Argonne National Laboratory, Argonne, Illinois 60439, United States; National Institute of Chemistry, SI-1000 Ljubljana, Slovenia; Faculty of Chemistry and Chemical Technology, University of Ljubljana, SI-1000 Ljubljana, Slovenia; [orcid.org/0000-0002-7078-0378](https://orcid.org/0000-0002-7078-0378)

**Pietro P. Lopes** – Materials Science Division, Argonne National Laboratory, Argonne, Illinois 60439, United States; [orcid.org/0000-0003-3211-470X](https://orcid.org/0000-0003-3211-470X)

**Brian Gould** – Materials Science Division, Argonne National Laboratory, Argonne, Illinois 60439, United States

**Filippo Maglia** – Battery Cell Technology, BMW Group, 80788 München, Germany; Institute for Advanced Study, Technical University of Munich, D-85748 Garching, Germany

**Roland Jung** – Battery Cell Technology, BMW Group, 80788 München, Germany; [orcid.org/0000-0003-1135-7438](https://orcid.org/0000-0003-1135-7438)

**Vojislav Stamenkovic** – Materials Science Division, Argonne National Laboratory, Argonne, Illinois 60439, United States; Department of Chemical and Biomolecular Engineering, Horiba Institute for Mobility and Connectivity, University of California Irvine, Irvine, California 92697, United States; [orcid.org/0000-0002-1149-3563](https://orcid.org/0000-0002-1149-3563)

**Ivano E. Castelli** – Department of Energy Conversion and Storage, Technical University of Denmark, DK-2800 Kgs. Lyngby, Denmark; [orcid.org/0000-0001-5880-5045](https://orcid.org/0000-0001-5880-5045)

**Nenad M. Markovic** – Materials Science Division, Argonne National Laboratory, Argonne, Illinois 60439, United States

**Jan Rossmeisl** – Nano-Science Center, Department of Chemistry, University of Copenhagen, DK-2100 Copenhagen, Denmark; [orcid.org/0000-0001-7749-6567](https://orcid.org/0000-0001-7749-6567)

Complete contact information is available at: <https://pubs.acs.org/doi/10.1021/acscatal.3c01531>

### Author Contributions

M.M. and D.S. conceived and designed the experiments. M.M., D.S., J.G.C., D.H., P.F.B.D.M., B.G., P.P.L., and B.G. performed the experiments. I.E.C., H.W., K.L.S., and J.R. performed the calculations. M.M., D.S., J.G.C., P.F.B.D.M., I.E.C., F.M., J.R., I.E.C., R.J., and N.M.M. discussed the results and wrote the paper.

### Notes

The authors declare no competing financial interest.

## ■ ACKNOWLEDGMENTS

This research was sponsored by BMW Technology Corporation. Support from Peter Faguy at the Vehicle Technologies Office (VTO), Office of Energy Efficiency and Renewable Energy, U.S. Department of Energy, is also gratefully acknowledged. The research was conducted at Argonne National Laboratory—a US Department of Energy Office of

Science laboratory operated by UChicago Argonne under contract number DE-AC02-06CH11357.

## REFERENCES

- (1) Goodenough, J. B.; Park, K. S. The Li-Ion Rechargeable Battery: A Perspective. *J. Am. Chem. Soc.* **2013**, *135*, 1167–1176.
- (2) Zubi, G.; Dufo-López, R.; Carvalho, M.; Pasaoglu, G. The Lithium-Ion Battery: State of the Art and Future Perspectives. *Renewable Sustainable Energy Rev.* **2018**, *89*, 292–308.
- (3) Palacín, M. R. Understanding Ageing in Li-Ion Batteries: A Chemical Issue. *Chem. Soc. Rev.* **2018**, *47*, 4924–4933.
- (4) Kabir, M. M.; Demirocak, D. E. Degradation Mechanisms in Li-Ion Batteries: A State-of-the-Art-Review. *Int. J. Energy Res.* **2017**, *41*, 1963–1986.
- (5) Etacheri, V.; Marom, R.; Elazari, R.; Salitra, G.; Aurbach, D. Challenges in the Development of Advanced Li-Ion Batteries: A Review. *Energy Environ. Sci.* **2011**, *4*, 3243–3262.
- (6) Gauthier, M.; Carney, T. J.; Grimaud, A.; Giordano, L.; Pour, N.; Chang, H. H.; Fenning, D. P.; Lux, S. F.; Paschos, O.; Bauer, C.; Maglia, F.; Lupart, S.; Lamp, P.; Shao-Horn, Y. Electrode-Electrolyte Interface in Li-Ion Batteries: Current Understanding and New Insights. *J. Phys. Chem. Lett.* **2015**, *6*, 4653–4672.
- (7) Edström, K.; Herstedt, M.; Abraham, D. P. A New Look at the Solid Electrolyte Interphase on Graphite Anodes in Li-Ion Batteries. *J. Power Sources* **2006**, *153*, 380–384.
- (8) Aurbach, D.; Zinigrad, E.; Cohen, Y.; Teller, H. A Short Review of Failure Mechanisms of Lithium Metal and Lithiated Graphite Anodes in Liquid Electrolyte Solutions. *Solid State Ionics* **2002**, *148*, 405–416.
- (9) Verma, P.; Maire, P.; Novák, P. A Review of the Features and Analyses of the Solid Electrolyte Interphase in Li-Ion Batteries. *Electrochim. Acta* **2010**, *55*, 6332–6341.
- (10) Soto, F. A.; Ma, Y.; Martinez De La Hoz, J. M.; Seminario, J. M.; Balbuena, P. B. Formation and Growth Mechanisms of Solid-Electrolyte Interphase Layers in Rechargeable Batteries. *Chem. Mater.* **2015**, *27*, 7990–8000.
- (11) Peled, E.; Menkin, S. Review—SEI: Past, Present and Future. *J. Electrochem. Soc.* **2017**, *164*, A1703–A1719.
- (12) An, S. J.; Li, J.; Daniel, C.; Mohanty, D.; Nagpure, S.; Wood, D. L. The State of Understanding of the Lithium-Ion-Battery Graphite Solid Electrolyte Interphase (SEI) and Its Relationship to Formation Cycling. *Carbon* **2016**, *105*, 52–76.
- (13) Xu, K. Electrolytes and Interphases in Li-Ion Batteries and Beyond. *Chem. Rev.* **2014**, *114*, 11503–11618.
- (14) Xu, K. Nonaqueous Liquid Electrolytes for Lithium-Based Rechargeable Batteries. *Chem. Rev.* **2004**, *104*, 4303–4418.
- (15) Zhang, S. S.; Jow, T. R.; Amine, K.; Henriksen, G. L. LiPF<sub>6</sub> ± EC ± EMC Electrolyte for Li-Ion Battery. *J. Power Sources* **2002**, *107*, 18–23.
- (16) Aurbach, D. Review of Selected Electrode-Solution Interactions Which Determine the Performance of Li and Li Ion Batteries. *J. Power Sources* **2000**, *89*, 206–218.
- (17) Wang, A.; Kadam, S.; Li, H.; Shi, S.; Qi, Y. Review on Modeling of the Anode Solid Electrolyte Interphase (SEI) for Lithium-Ion Batteries. *npj Comput. Mater.* **2018**, *4*, 15.
- (18) Liu, T.; Lin, L.; Bi, X.; Tian, L.; Yang, K.; Liu, J.; Li, M.; Chen, Z.; Lu, J.; Amine, K.; Xu, K.; Pan, F. In Situ Quantification of Interphasial Chemistry in Li-Ion Battery. *Nat. Nanotechnol.* **2019**, *14*, 50–56.
- (19) Gogoi, N.; Melin, T.; Berg, E. J. Elucidating the Step-Wise Solid Electrolyte Interphase Formation in Lithium-Ion Batteries with Operando Raman Spectroscopy. *Adv. Mater. Interfaces* **2022**, *9*, 2200945.
- (20) Leroy, S.; Martinez, H.; Dedryvère, R.; Lemordant, D.; Gonbeau, D. Influence of the Lithium Salt Nature over the Surface Film Formation on a Graphite Electrode in Li-Ion Batteries: An XPS Study. *Appl. Surf. Sci.* **2007**, *253*, 4895–4905.
- (21) Chattopadhyay, S.; Lipson, A. L.; Karmel, H. J.; Emery, J. D.; Fister, T. T.; Fenter, P. A.; Hersam, M. C.; Bedzyk, M. In Situ X-ray Study of the Solid Electrolyte Interphase (SEI) Formation on Graphene as a Model Li-ion Battery Anode. *Chem. Mater.* **2012**, *24*, 3038–3043.
- (22) Owejan, J. E.; Owejan, J. P.; Decaluwe, S. C.; Dura, J. A. Solid Electrolyte Interphase in Li-Ion Batteries: Evolving Structures Measured in Situ by Neutron Reflectometry. *Chem. Mater.* **2012**, *24*, 2133–2140.
- (23) Leroy, S.; Blanchard, F.; Dedryvère, R.; Martinez, H.; Carré, B.; Lemordant, D.; Gonbeau, D. Surface Film Formation on a Graphite Electrode in Li-Ion Batteries: AFM and XPS Study. *Surf. Interface Anal.* **2005**, *37*, 773–781.
- (24) Adenusi, H.; Chass, G. A.; Passerini, S.; Tian, K. V.; Chen, G. Lithium Batteries and the Solid Electrolyte Interphase (SEI)—Progress and Outlook. *Adv. Energy Mater.* **2023**, *13*, 2203307.
- (25) Wang, L.; Menakath, A.; Han, F.; Wang, Y.; Zavalij, P. Y.; Gaskell, K. J.; Borodin, O.; Iuga, D.; Brown, S. P.; Wang, C.; Xu, K.; Eichhorn, B. W. Identifying the Components of the Solid–Electrolyte Interphase in Li-Ion Batteries. *Nat. Chem.* **2019**, *11*, 789–796.
- (26) Peled, E.; Bar Tow, D.; Merson, A.; Gladkikh, A.; Burstein, L.; Golodnitsky, D. Composition, Depth Profiles and Lateral Distribution of Materials in the SEI Built on HOPG-TOF SIMS and XPS Studies. *J. Power Sources* **2001**, *97–98*, 52–57.
- (27) Tsubouchi, S.; Domi, Y.; Doi, T.; Ochida, M.; Nakagawa, H.; Yamanaka, T.; Abe, T.; Ogumi, Z. Spectroscopic Characterization of Surface Films Formed on Edge Plane Graphite in Ethylene Carbonate-Based Electrolytes Containing Film-Forming Additives. *J. Electrochem. Soc.* **2012**, *159*, A1786–A1790.
- (28) Heiskanen, S. K.; Kim, J.; Lucht, B. L. Generation and Evolution of the Solid Electrolyte Interphase of Lithium-Ion Batteries. *Joule* **2019**, *3*, 2322–2333.
- (29) Cao, C.; Pollard, T. P.; Borodin, O.; Mars, J. E.; Tsao, Y.; Lukatskaya, M. R.; Kasse, R. M.; Schroeder, M. A.; Xu, K.; Toney, M. F.; Steinrück, H. G. Toward Unraveling the Origin of Lithium Fluoride in the Solid Electrolyte Interphase. *Chem. Mater.* **2021**, *33*, 7315–7336.
- (30) Borodin, O.; Ren, X.; Vatamanu, J.; Von Wald Cresce, A.; Knap, J.; Xu, K. Modeling Insight into Battery Electrolyte Electrochemical Stability and Interfacial Structure. *Acc. Chem. Res.* **2017**, *50*, 2886–2894.
- (31) Strmcnik, D.; Castelli, I. E.; Connell, J. G.; Haering, D.; Zorko, M.; Martins, P.; Lopes, P. P.; Genorio, B.; Østergaard, T.; Gasteiger, H. A.; Maglia, F.; Antonopoulos, B. K.; Stamenkovic, V. R.; Rossmeisl, J.; Markovic, N. M. Electrocatalytic Transformation of HF Impurity to H<sub>2</sub> and LiF in Lithium-Ion Batteries. *Nat. Catal.* **2018**, *1*, 255–262.
- (32) Castelli, I. E.; Zorko, M.; Østergaard, T. M.; Martins, P. F. B. D.; Lopes, P. P.; Antonopoulos, B. K.; Maglia, F.; Markovic, N. M.; Strmcnik, D.; Rossmeisl, J. The Role of an Interface in Stabilizing Reaction Intermediates for Hydrogen Evolution in Aprotic Electrolytes. *Chem. Sci.* **2020**, *11*, 3914–3922.
- (33) Pasierb, P.; Komornicki, S.; Rokita, M.; Rękas, M. Structural Properties of Li<sub>2</sub>CO<sub>3</sub>-BaCO<sub>3</sub> System Derived from IR and Raman Spectroscopy. *J. Mol. Struct.* **2001**, *596*, 151–156.
- (34) Wijaya, O.; Hartmann, P.; Younesi, R.; Markovits, I. I. E.; Rinaldi, A.; Janek, J.; Yazami, R. A Gamma Fluorinated Ether as an Additive for Enhanced Oxygen Activity in Li-O<sub>2</sub> Batteries. *J. Mater. Chem. A* **2015**, *3*, 19061–19067.
- (35) Zhuang, G. V.; Xu, K.; Yang, H.; Jow, T. R.; Ross, P. N. Lithium Ethylene Dicarboxylate Identified as the Primary Product of Chemical and Electrochemical Reduction of EC in 1.2 M LiPF<sub>6</sub> / EC:EMC Electrolyte. *J. Phys. Chem. B* **2005**, *109*, 17567–17573.
- (36) Lanz, P.; Novák, P. Combined In Situ Raman and IR Microscopy at the Interface of a Single Graphite Particle with Ethylene Carbonate/Dimethyl Carbonate. *J. Electrochem. Soc.* **2014**, *161*, A1555–A1563.
- (37) Onuki, M.; Kinoshita, S.; Sakata, Y.; Yanagidate, M.; Otake, Y.; Ue, M.; Deguchi, M. Identification of the Source of Evolved Gas in Li-Ion Batteries Using [Sup 13]C-Labeled Solvents. *J. Electrochem. Soc.* **2008**, *155*, A794.



- (38) Zhuang, G. V.; Yang, H.; Bliznac, B.; Ross, P. N. A Study of Electrochemical Reduction of Ethylene and Propylene Carbonate Electrolytes on Graphite Using ATR-FTIR Spectroscopy. *Electrochem. Solid-State Lett.* **2005**, *8*, 441–445.
- (39) Strehle, B.; Solchenbach, S.; Metzger, M.; Schwenke, K. U.; Gasteiger, H. A. The Effect of CO<sub>2</sub> on Alkyl Carbonate Trans-Esterification during Formation of Graphite Electrodes in Li-Ion Batteries. *J. Electrochem. Soc.* **2017**, *164*, A2513–A2526.
- (40) Bedrov, D.; Smith, G. D.; Van Duin, A. C. T. Reactions of Singly-Reduced Ethylene Carbonate in Lithium Battery Electrolytes: A Molecular Dynamics Simulation Study Using the ReaxFF. *J. Phys. Chem. A* **2012**, *116*, 2978–2985.
- (41) Metzger, M.; Strehle, B.; Solchenbach, S.; Gasteiger, H. A. Hydrolysis of Ethylene Carbonate with Water and Hydroxide under Battery Operating Conditions. *J. Electrochem. Soc.* **2016**, *163*, A1219–A1225.
- (42) Matsuoka, O.; Hiwara, A.; Omi, T.; Toriida, M.; Hayashi, T.; Tanaka, C.; Saito, Y.; Ishida, T.; Tan, H.; Ono, S. S.; Yamamoto, S. Ultra-Thin Passivating Film Induced by Vinylene Carbonate on Highly Oriented Pyrolytic Graphite Negative Electrode in Lithium-Ion Cell. *J. Power Sources* **2002**, *108*, 128–138.
- (43) Jeong, S.-K.; Inaba, M.; Abe, T.; Ogumi, Z. Surface Film Formation on Graphite Negative Electrode in Lithium-Ion Batteries: AFM Study in an Ethylene Carbonate-Based Solution. *J. Electrochem. Soc.* **2001**, *148*, A989.
- (44) Inaba, M.; Siroma, Z.; Funabiki, A.; Ogumi, Z.; Abe, T.; Mizutani, Y.; Asano, M. Electrochemical Scanning Tunneling Microscopy Observation of Highly Oriented Pyrolytic Graphite Surface Reactions in an Ethylene Carbonate-Based Electrolyte Solution. *Langmuir* **1996**, *12*, 1535–1540.
- (45) Domi, Y.; Ochida, M.; Tsubouchi, S.; Nakagawa, H.; Yamanaka, T.; Doi, T.; Abe, T.; Ogumi, Z. Electrochemical AFM Observation of the HOPG Edge Plane in Ethylene Carbonate-Based Electrolytes Containing Film-Forming Additives. *J. Electrochem. Soc.* **2012**, *159*, A1292–A1297.
- (46) Domi, Y.; Ochida, M.; Tsubouchi, S.; Nakagawa, H.; Yamanaka, T.; Doi, T.; Abe, T.; Ogumi, Z. In Situ AFM Study of Surface Film Formation on the Edge Plane of HOPG for Lithium-Ion Batteries. *J. Phys. Chem. C* **2011**, *115*, 25484–25489.
- (47) Alliata, D.; Kötz, R.; Novák, P.; Siegenthaler, H. Electrochemical SPM Investigation of the Solid Electrolyte Interphase Film Formed on HOPG Electrodes. *Electrochem. Commun.* **2000**, *2*, 436–440.
- (48) Lux, S. F.; Lucas, I. T.; Pollak, E.; Passerini, S.; Winter, M.; Kostecki, R. The Mechanism of HF Formation in LiPF<sub>6</sub> Based Organic Carbonate Electrolytes. *Electrochem. Commun.* **2012**, *14*, 47–50.
- (49) Plakhotnyk, A. V.; Ernst, L.; Schmutzler, R. Hydrolysis in the System LiPF<sub>6</sub> - Propylene Carbonate - Dimethyl Carbonate - H<sub>2</sub>O. *J. Fluorine Chem.* **2005**, *126*, 27–31.
- (50) Tsiouvaras, N.; Meini, S.; Buchberger, I.; Gasteiger, H. A. A Novel On-Line Mass Spectrometer Design for the Study of Multiple Charging Cycles of a Li-O<sub>2</sub> Battery. *J. Electrochem. Soc.* **2013**, *160*, A471–A477.
- (51) Metzger, M.; Strehle, B.; Solchenbach, S.; Gasteiger, H. A. Origin of H<sub>2</sub> Evolution in LIBs: H<sub>2</sub>O Reduction vs. Electrolyte Oxidation. *J. Electrochem. Soc.* **2016**, *163*, A798–A809.
- (52) Enkovaara, J.; Rostgaard, C.; Mortensen, J. J.; Chen, J.; Dulak, M.; Ferrighi, L.; Gavnholt, J.; Glinzvad, C.; Haikola, V.; Hansen, H. A.; Kristoffersen, H. H.; Kuisma, M.; Larsen, A. H.; Lehtovaara, L.; Ljungberg, M.; Lopez-Acevedo, O.; Moses, P. G.; Ojanen, J.; Olsen, T.; Petzold, V.; Romero, N. A.; Stausholm-Møller, J.; Strange, M.; Tritsaris, G. A.; Vanin, M.; Walter, M.; Hammer, B.; Häkkinen, H.; Madsen, G. K. H.; Nieminen, R. M.; Nørskov, J. K.; Puska, M.; Rantala, T. T.; Schiøtz, J.; Thygesen, K. S.; Jacobsen, K. W. Electronic Structure Calculations with GPAW: A Real-Space Implementation of the Projector Augmented-Wave Method. *J. Phys.: Condens. Matter* **2010**, *22*, 253202.
- (53) Mortensen, J. J.; Hansen, L. B.; Jacobsen, K. W. Real-Space Grid Implementation of the Projector Augmented Wave Method. *Phys. Rev. B: Condens. Matter Mater. Phys.* **2005**, *71*, 035109.
- (54) Larsen, A. H. The Atomic Simulation Environment - A Python Library for Working with Atoms. *J. Phys.: Condens. Matter* **2017**, *29*, 273002.
- (55) Hammer, B.; Hansen, L. B.; Nørskov, J. K. Improved Adsorption Energetics within Density-Functional Theory Using Revised Perdew-Burke-Ernzerhof Functionals. *Phys. Rev. B: Condens. Matter Mater. Phys.* **1999**, *59*, 7413–7421.

## Recommended by ACS

### A Joint DFT-kMC Study To Model Ethylene Carbonate Decomposition Reactions: SEI Formation, Growth, and Capacity Loss during Calendar Aging of Li-Metal Batteries

Mohammed Bin Jassar, Stephan N. Steinmann, *et al.*

JUNE 26, 2023

ACS APPLIED ENERGY MATERIALS

READ 

### Weak Solvent–Solvent Interaction Enables High Stability of Battery Electrolyte

Yuqi Wang, Jun Ming, *et al.*

FEBRUARY 17, 2023

ACS ENERGY LETTERS

READ 

### First-Principles Examination of Multiple Criteria of Organic Solvent Oxidative Stability in Batteries

Kevin Leung.

MARCH 08, 2023

CHEMISTRY OF MATERIALS

READ 

### Effect of the Electric Double Layer (EDL) in Multicomponent Electrolyte Reduction and Solid Electrolyte Interphase (SEI) Formation in Lithium Batteries

Qisheng Wu, Yue Qi, *et al.*

JANUARY 23, 2023

JOURNAL OF THE AMERICAN CHEMICAL SOCIETY

READ 

Get More Suggestions >